Nuclear Instruments and Methods in Physics Research B 383 (2016) 21–37

Contents lists available at ScienceDirect

Nuclear Instruments and Methods in Physics Research B

journal homepage: www.elsevier.com/locate/nimb

Experimental investigation of the radiation shielding efficiency of a MCP detector in the radiation environment near Jupiter's moon Europa

M. Tulej [a,*], S. Meyer [a], M. Lüthi [a], D. Lasi [a], A. Galli [a], D. Piazza [a], L. Desorgher [b], D. Reggiani [b], W. Hajdas [b], S. Karlsson [c], L. Kalla [c], P. Wurz [a]

[a] Space Research and Planetary Sciences, Physics Institute, University of Bern, CH-3012 Bern, Switzerland
[b] Laboratory of Particle Physics, Paul Scherrer Institute, CH-5232, Villigen, Switzerland
[c] Swedish Institute of Space Physics, Space Kampus 1, Kiruna, Sweden

ARTICLE INFO

Article history:
Received 3 March 2016
Received in revised form 13 June 2016
Accepted 15 June 2016

Keywords:
Electron beam
Radiation shielding
GEANT4
GRAS
Radiation effects
JUICE
MCP detector

ABSTRACT

Neutral Ion Mass spectrometer (NIM) is one of the instruments in the Particle Environmental Package (PEP) designed for the JUICE mission of ESA to the Jupiter system. NIM, equipped with a sensitive MCP ion detector, will conduct detailed measurements of the chemical composition of Jovian icy moons exospheres. To achieve high sensitivity of the instrument, radiation effects due to the high radiation background (high-energy electrons and protons) around Jupiter have to be minimised. We investigate the performance of an Al–Ta–Al composite stack as a potential shielding against high-energy electrons. Experiments were performed at the PiM1 beam line of the High Intensity Proton Accelerator Facilities located at the Paul Scherrer Institute, Villigen, Switzerland. The facility delivers a particle beam containing e^-, μ^- and π^- with momentum from 17.5 to 345 MeV/c (Hajdas et al., 2014). The measurements of the radiation environment generated during the interaction of primary particles with the Al–Ta–Al material were conducted with dedicated beam diagnostic methods and with the NIM MCP detector. In parallel, modelling studies using GEANT4 and GRAS suites were performed to identify products of the interaction and predict ultimate fluxes and particle rates at the MCP detector. Combination of experiment and modelling studies yields detailed characterisation of the radiation fields produced by the interaction of the incident e^- with the shielding material in the range of the beam momentum from 17.5 to 345 MeV/c. We derived the effective MCP detection efficiency to primary and secondary radiation and effective shielding transmission coefficients to incident high-energy electron beam in the range of applied beam momenta. This study shows that the applied shielding attenuates efficiently high-energy electrons. Nevertheless, owing to nearly linear increase of the bremsstrahlung production rate with incident beam energy, above 130 MeV their detection rates measured by the MCP detector compares to the MCP rate of the incident electron beam. We define key performance parameters for the shielding and show direction of its improvements by introducing additional layer of material to attenuate γ-rays and reduce the MCP sensitivity to the penetrating radiation. The experiments also verify the predictions by modelling tools used currently for optimisation of shielding against high-energy particles.

1. Introduction

The Jupiter Icy Moons Explorer (JUICE) mission to explore the Jupiter system is an L-class mission of ESA to be launched in 2022 [1–3]. The spacecraft will be equipped with the Particle Environmental Package (PEP) containing six sensors that will measure the magnetosphere of Jupiter and the exospheres of its icy moons Europa, Ganymede, and Callisto. The Neutral Ion Mass spectrometer (NIM), one of the PEP sensors accommodated on the JUICE spacecraft nadir face, will perform the first-ever direct sampling of neutral gas and thermal plasma surrounding the icy satellites during the flybys of Europa, Ganymede, and Callisto, and during the orbits around Ganymede.

The NIM instrument has a compact design based on the time-of-flight (TOF) principle and uses a sensitive MCP ion detector [4,5]. The mass spectrometer can record spectra in the mass range 1–1000 amu, with a mass resolution (M/ΔM) ~1100 and a field of view (FOV) of 10° × 360°. The instrument supports 6 decades (10^6) dynamic range and can deliver highly sensitive measurements of

* Corresponding author.
E-mail address: marek.tulej@space.unibe.ch (M. Tulej).

http://dx.doi.org/10.1016/j.nimb.2016.06.008
0168-583X/

chemical composition of molecular, atomic and isotope species of the exospheric gases [2–4,6]. Highly sensitive measurements are essential and can address many scientific questions about the habitability of these moons [7,8]. At Europa, however, where JUICE will encounter the most demanding environment in terms of high energy radiation fluxes, the detection threshold of NIM is estimated to increase from ~2 to 30 cm^{-3} s^{-1} because of the high level of penetrating radiation due to high-energy electrons and protons. The penetrating radiation can reduce severely performance of the instrument by increasing noise level, causing detector saturation effects, and reducing detectors lifetime [9,10]. Hence, high radiation tolerance of the instrument components is required [11].

The NIM ion detector contains microchannel plates (MCPs) with the highest detection efficiency (~70%) to particles with energies in the range of few keV [12–15]. The MCP detection efficiencies were investigated also for more energetic electrons in the range of some tenths of keV to hundredths of MeV [16–19]. A trend of decreasing MCP detection efficiencies to electrons with higher energies is observed. The detection efficiency for energetic electrons in the Jovian environment is expected to be 5–6% at least in the energy range 1–350 MeV and their high-rate can generate considerable background noise [18,19]. To reduce this noise the MCP detector has to be appropriately shielded [19]. Parallel to the attenuation of the primary particle flux also the secondary radiation produced in the shielding (secondary electrons, γ-rays) has to be reduced [20]. In the present modelling studies of the shielding protecting the MCP detector in the NIM instrument, the geometry and shielding thickness based on an Al–Ta–Al composite stack was derived taking into account the energetic electron fluxes expected near Jupiter [7]. The shielding design considered here represents the passive radiation shielding for NIM and was optimised for the measurements planned for the Europa flybys, which represent the worst case radiation scenario for the JUICE mission [40].

In the present study, we have developed a measurement methodology allowing for a detailed analysis of radiation effects produced by high-rate and high-energy particles penetrating shielding material. We characterise the parameters of the incident particle beam and radiation effects produced by the interaction of primary beam with the shielding material by several beam diagnostic techniques using appropriate particle detectors. Measurements with the MCP detector are referenced to the results obtained from the beam diagnostic studies. In parallel, the modelling of the interaction of the primary particle beam with the shielding material was conducted to understand the composition of secondary radiation (radiation effects) behind the shielding. Both modelling results and the MCP measurements yield beam transmission coefficients as a function of the primary beam energy. The measurement method leads to the quantitative characterisation of radiation fields produced by incident particles in the shielding material. The effective MCP detection efficiency to secondary products provide the input to improve the design of the shielding.

2. Experimental method

2.1. Secondary beam line of the PSI High Intensity Proton Accelerator

The experimental studies were conducted at the High Intensity Proton Accelerator Facility, PSI Villigen, Switzerland with the secondary beamline, PiM1 [21]. In the current application, the PiM1 beamline is optimised to deliver electrons (e^-), pions (π^-), and muons (μ^-) to the experimental area. The momenta of these particles can be selected in the range 11.5–345 MeV/c by tuning the magnet of the beam delivery system [21]. The quadrupole and dipole magnets of the PiM1 beamline transport the particles to the experimental area, where the beam is focused by two magnetic quadrupoles located near the experimental arrangement. The length of the whole beam line from the particle production target to the focus point is 23.65 m. Because there are no electrostatic separators the PiM1 beam always contains a mixture of e^-, μ^- and π^- particles having the same momentum.

2.2. Shielding arrangement

For the present investigations, two separate shielding sets were prepared from certified Al (Alloy 6082; Al 99%, Si 1%) materials and Ta (To-226; Nr. 112426 Hainess–Maassen). The first was used in the experiments with the beam diagnostic instruments, and was made of rectangular plates (200 mm × 200 mm) arranged as an Al (1 mm) Ta (10 mm) Al (1 mm) sandwich (Fig. 1). The second was mounted behind the Al (2 mm) entrance window of the vacuum chamber containing the MCP detector, and was made of a circular (Ø 50 mm) Ta (10 mm) Al (1 mm) composite stack. In summary, the shielding stack had a very similar composition in both the experiments performed with the beam diagnostic instrument and with the MCP detector, the only difference being that for the MCP experiment the outermost Al layer of the shielding (i.e., the first encountered by the beam) was 2 instead of 1 mm thick due to construction constraints. Because in the actual flight detector of the NIM instrument, the MCP will be encapsulated inside a shielding cage, an identical round shielding element was mounted on the opposite window of the vacuum chamber to account for any effect due to backscattering. In all measurements, the shielding assembly that is facing the beam was located at the centre of the beam focal plane (Fig. 1).

2.3. Diagnostic instrumentation

The experimental characterisation of the primary (incident) and secondary particle beams (produced after the primary particles passed the shielding) was achieved with four methods: (i) a ΔE–E plastic scintillator telescope, (ii) a NaI(Tl) scintillation detector, (iii) a parallel plate ionisation chamber, and (iv) a beam scanner. The ionisation chamber was inserted just behind the beam exit from the vacuum pipe. The beam telescope consists of a ΔE thin plastic (30 mm × 30 mm × 2 mm) and a cylindrically-shaped E detector (30 mm thick, Ø 28 mm). Both detectors were separated by ~5 mm. The telescope located at the focal position was applied to identify primary and secondary electrons using coincidence and anticoincidence methods. The NaI(Tl) scintillation detector (1″ thick, Ø 1″) was used for γ-ray measurements. The beam scanner with a plastic scintillator (2 × 2 mm^2) was mounted on the XY-translation table to acquire the 2D beam profile. A scintillator detector at the centre of the beam at its focal plane determined the beam flux maximum.

The readout electronics was located in a separate room, several meters away from the measurement area [19]. The signals produced by the ionisation chamber were registered by a high-precision pico-amperemeter with current-to-voltage and voltage-to-frequency converters and a counter. The plastic telescope delivered signals to a linear (analogue) fan-out followed on one output by amplitude discriminators, a logical coincidence unit, and counters. A high-speed oscilloscope was employed for the output signal and wave detection for time-resolved pulse analysis including histograms for signal amplitudes and time differences with respect to trigger and storage of data. The signals from the NaI(Tl) detector were sent to the preamplifier and amplifier, and were then analysed by the multi-channel analyser. Signals from the beam scanner produced by a small scintillator together with the main accelerator beam monitor were fed to a DRS4 chip evaluation board working as a discriminator and a counter. All high voltage power supplies for

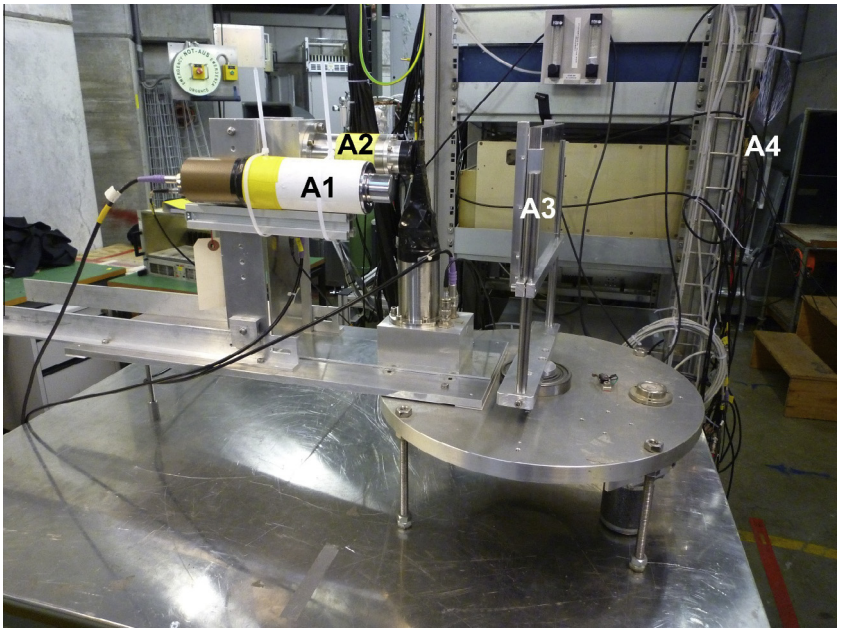

Fig. 1. Experimental setup for the beam diagnostic measurements A1: E−ΔE plastic scintillator telescope, A2: NaI(Tl) scintillation detector for γ-rays detection; A3: Al/Ta/Al shielding; A4: support electronics.

the above detectors were located directly in the PiM1 area; the measurements were remotely controlled from the control room [19]. Initially all detectors were calibrated with radioactive sources.

The beam composition was analysed with TOF and energy-loss methods [21]. In the TOF method, the arrival times of e^-, μ^- and π^- particles from the production target to the MCP detector were measured. The measurements were synchronised with the phase of the 50 MHz accelerator radiofrequency signal. A small scanning detector inserted at the beam focal plane provided the start signal, and the 50 MHz synchrocyclotron waveform provided the stop signal. In the range of applied beam momenta, the electrons travel with nearly speed of light. Therefore, their times of arrival at the detector are relatively independent on beam momentum. However, for π^- and μ^- the times of arrival are momentum-dependent, and these particles arrive with some delays compared to electrons. The three temporally separated groups of peaks can be measured as a function of beam momentum. Analysis of the signals determined the particle beam fractions. The analysis of the beam composition with the energy-loss method allowed us to confirm the results obtained with the TOF method.

2.4. Experimental setup for the measurements with MCP detector

The experimental setup for the measurements with the MCP detector is similar to that described in our recent publication [19], the only difference being the implementation of the shielding described in Section 2.2. The same MCP detector as in the investigations of MCP detection efficiency is applied in the present studies. The relevant electric circuit and the detailed characteristics of the MCP plates applied in the detector are described in our recent publication [19]. Two 0.6 mm thick MCP wafers (arranged in Chevron configuration, made of lead glass, with a channel diameter of 10 μm and channel pitch 12 μm were assembled to form amplification stages of $\sim 10^4$ and $\sim 10^3$ in the front and second MCP plates, respectively. The high voltage operation can be arranged in the voltage range 1700–2100 V. In the present experiments, the voltage of 1900 V was applied between MCPs. The channels in MCPs have a bias angle to the normal axes of 8°. The MCP assembly was combined with a custom-made high-frequency anode coupled to a 50 Ω transmission line. Anode signals were sampled on a 50 Ω load with an R&S®RTO1024 oscilloscope, providing an 8-bit digitisation of the waveforms at 10 GSPS with an input bandwidth of 2 GHz. Measurements of individual waveforms were triggered when a pulse signal with an amplitude smaller than $|V| = 2.5$ mV was produced by the MCP detector [19].

The MCP detector was kept in a cylindrical stainless steel vacuum chamber, which was pumped down to pressures lower than 10^{-6} mbar by turbo-molecular and rotary pumps. The detector is mounted on a rotating rod to vary the angle of incidence with the particle beam in the range of incidence angles 0–180°. The MCP detector could be rotated in both left/right directions with respect to 0° angle. To distinguish between the MCP orientations towards incident beam direction the angles are indicated with ±signs (Fig. 2a). The incident beam was always positioned at 0° to the shielding normal axes, and only the detector is allowed to rotate. The circular entrance window was made from a composite stack of Al (2 mm), Ta (10 mm) and Al (1 mm) plates, 50 mm diameter each. The distance from the MCP detector to the beam focal location was 45 mm and the effective distance from the rear Al plate of the radiation shielding to the front MCP plate was ~32 mm (Fig. 2b). The particle beam was aligned collinearly with the centre of MCP plates and its diameter, precisely measured with the beam scanner, was larger than the MCP effective diameter (8 mm).

2.5. Measurement method

Two kinds of experimental investigations were performed, including the beam diagnostic studies and the measurements of the particle beam by the MCP detector. The beam diagnostic studies provided beam characteristics including particle fractions, beam geometry, beam fluxes, and beam intensity as function of the beam momentum. The MCP detector detected the incident particles with a high temporal resolution delivering the particle rate measurements. The diagnostic measurements provided the calibration of the MCP measurements necessary to conduct the quantitative analysis by this experiment. By combining the analysis of

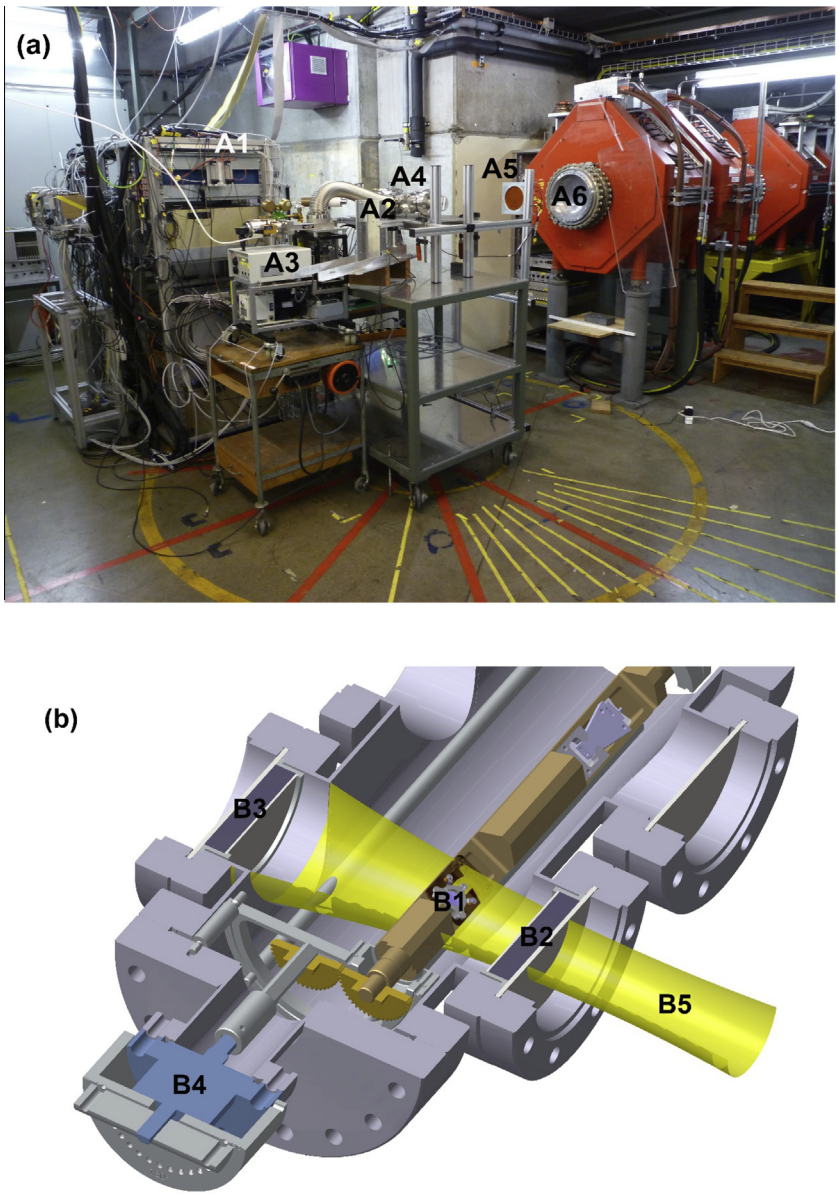

Fig. 2. (a) An overview of the experimental setup: electronic rack A1, beam diagnostic instruments A2, vacuum system A3, vacuum chamber containing the MCP detector A4, ionisation chamber A5, exit window of PiM1 beamline A6. (b) Cut through the design drawing of the experimental vacuum chamber (stainless steel; SS) with a schematic envelope of the particle beam penetrating the vacuum chamber: the MCP detector B1 kept by housing (PEEK material) on a glass fibre reinforced plastics GFRP (FR4), entrance window B2, rear window B3 (10 mm Ta + 3 mm Al), and rotating assembly B4; shape of the incident particle and secondary particle beam (yellow tubular feature) B5. (For interpretation of the references to colour in this figure legend, the reader is referred to the web version of this article.)

the measurements by the MCP detector and the results of the modelling, a detailed radiation compositional analysis was performed. In our recent publication, that analysis led to the determination of the MCP detection efficiencies to e^- and π^- [19]. In the present study, the properties of the radiation shielding are investigated by measurements of the radiation environment produced by the incident particle beam as a function of beam momentum.

Shielding not only reduces incident particle flux but also produces a number of various secondary particles to which the MCP detector can be sensitive depending on their charge and energy. We therefore introduce a shielding dependent MCP detection efficiency, $\eta_{S/NS}(P_i)$, in the function of the momentum (P_i) which we also call the effective MCP detection efficiency. It is defined as the ratio of the secondary (and transmitted primaries if present) particle rate measured by the MCP detector, $k_S^{MCP}(P_i)$, to the incident particle rate, $k_{NS}(P_i)$ (the rate of incident particles at the front MCP surface when no shielding is applied):

$$\eta_{S/NS}(P_i) = \frac{k_S^{MCP}(P_i)}{k_{NS}(P_i)} \quad (1)$$

The $\eta_{S/NS}$ coefficient is a measure of the MCP detector efficiency to the radiation field produced by the interaction of the incident particles with the shielding material. Knowing the MCP detection efficiency to the incident particles we can characterise also the performance of the shielding to attenuate the incident particle beam. We define the effective beam transmission coefficient, $T(P_i)$ for the shielding as the ratio of the rate of the secondary particles (and transmitted primaries) measured by the MCP detector, $k_S^{MCP}(P_i)$, [#counts/s] to the rate of incident particle which will be measured by the MCP detector, $k_{NS}^{MCP}(P_i)$ at the applied beam momentum, P_i:

$$T(P_i) = \frac{k_S^{MCP}(P_i)}{k_{NS}^{MCP}(P_i)} = \frac{k_S^{MCP}(P_i)}{\eta(P_i) * k_{NS}(P_i)} \quad (2)$$

The latter rate is determined by the incident particle rate at the front MCP and the MCP detection efficiency to the incident particles: $k_{NS}^{MCP}(P_i) = \eta(P_i)^* k_{NS}(P_i)$, [#counts/s]. For $T = 1$, the rate of secondary particles is equivalent to the rate of incident particles and the shielding is considered transparent. For $T < 1$ the beam is attenuated and for $T > 1$ the incident beam is amplified by the shielding.

In the present study we investigated the radiation environment induced by the primary electrons. The results of analyses of radiation effects induced by the interaction of π^- with shielding were used to support these analyses and help in the beam compositional analysis.

We also performed detailed studies with GEANT4 (GEometry And Tracking) and GRAS (Geant4 Radiation Analysis for Space) to model the interaction of primary beams (e^-, μ^-, and π^-) with the shielding material, using the measured primary beam characteristics as input parameters and the details of the MCP shielding arrangement to enable direct comparison with the MCP measurement results. We accounted for the attenuation of the primary beam and the production of secondary particles. The modelling results provided fluxes and beam intensities of secondary particles for the range of investigated beam momenta and form the basis for a detailed beam compositional analysis. The experimental results also provide a test case for the performance of the theoretical models.

3. Results and discussion

3.1. Beam diagnostic studies

3.1.1. Composition of primary and secondary beams

The e^-, μ^- and π^- particles are produced during the interaction of primary proton beam with a carbon target. In the range of applied beam momenta, the electrons are relativistic and arrived at the experimental area at similar times. For the other heavier particles, time-of-flights are longer and are the function of the momentum. For the beam momenta lower than 115 MeV/c, only electrons are detectable. For larger beam momenta three groups of well-resolved peaks are observed in TOF histograms. They can be assigned to e^-, μ^- and π^- particles based on time-of-flight (TOF) analysis [21]. Relative fractions of e^-, μ^- and π^- are obtained by integrating relevant peak intensity and dividing by the sum of all integrated peaks (Table 1).

Table 1
The beam momentum (p), kinetic energy (T), and beam fractions of the e^-, μ^-, and π^- determined from the TOF measurements. The relativistic E–p transformation is applied to make the conversion between E (total energy) and p: $E^2 = p^2c^2 + (m_0c^2)^2$ and $E = T + m_0c^2$. Here m_0 is the rest mass of relevant particle. The m_0c^2 values are 0.511, 105.658 and 139.57 MeV for e^-, μ^- and π^-, respectively.

Beam momentum [MeV/c]	Kinetic energy [MeV]			Fraction [%]		
	e^-	μ^-	π^-	e^-	μ^-	π^-
17.25	16.746	1.399	1.062	100	0	0
23	22.494	2.474	1.882	100	0	0
28.75	28.243	3.842	2.930	100	0	0
57.5	56.990	14.633	11.380	100	0	0
86.25	85.740	30.734	24.500	100	0	0
115	114.489	50.511	41.275	97.46	0.67	1.87
143.75	143.26	72.748	60.789	83.77	2.07	14.16
172.5	171.989	96.629	82.322	63.16	2.37	34.47
201.25	200.79	121.646	105.341	46.44	2.15	51.41
230	229.489	147.450	129.465	30.44	0	69.56
287.5	286.988	200.642	180.017	13.96	0	86.04
345	344.488	255.159	232.592	6.9	0	93.1

The characterisation of the secondary beam produced by the interaction of the primary particles with shielding is achieved by applying coincidence and anti-coincidence methods. Fig. 3 shows a few typical spectra measured by diagnostic instruments. The spectra were measured with a thin, cylindrically-shaped E detector located 130 mm behind the shielding plane (beam focal plane). The measurements are indicative of large γ-ray production rate (the signal due to γ-rays dominates the secondary particle spectra). The fraction of the incident electrons is reduced in the beam by about two orders of magnitude.

The primary beam coincidence spectrum measured with a ΔE−E plastic detector (telescope) is presented in Fig. 4a. The envelope of both detectors is similar, but one cannot exclude some contamination by electrons through the coincidence system of the telescope, which would affect to some extent the magnitude of the measured signals. In this measurement a telescope made of a thin plastic ($30 \times 28 \times 2$ mm^3) and a thick cylinder (Ø 28 mm, 30 mm thick) E-detector separated by 1 cm gap was used.

The same telescope was used to measure secondary particles and γ-rays behind the shielding. The system was set either for a coincidence to measure charged particles or for anti-coincidence for measurement of γ-rays (Fig. 4b). The anti-coincidence events are observed readily in the spectra. Nevertheless, the detections were not 100% efficient and the measurements will further require a careful modelling and improvements of the test setup to improve the quantitative analysis of the beam composition. The coincidence spectrum indicates that some primary electrons are transmitted also through the shielding. The peak seen around 7 MeV corresponds to the energy loss of such relativistic electrons in the (30 mm thick) plastic cylinder.

3.1.2. Primary and secondary beam profiles

The spatial beam intensity (flux) profiles were measured by the beam scanner with a small (Ø 5 mm) plastic scintillator detector. The measurements were conducted both at the beam focal plane and about 130 mm behind it, while the shielding was inserted at the focal plane location. Vertical and horizontal scans of the beam profiles were performed in the beam momenta range from 17 MeV/c to 345 MeV/c. All recorded profiles were fitted with a Gauss-function to determine a beam waist (FWHM) and centre position for both directions. A scintillator detector inserted in the beam centre measured the maximal beam flux. The beam parameters derived from both measurements for the whole range of the applied beam momenta are presented in Fig. 5.

The measurements show that the position of the beam centre varied to some extent but not significantly (Fig. 5a). At the beam focal plane, the planar shape of the beam is close to ellipsoid and the beam size (σ_x, σ_y) depends readily on the beam momentum (Fig. 5b). For the measurements without shielding an increase of the beam size for low beam momenta is attributed to increase of the beam scattering cross section with the air. A significantly larger beam size is measured approximately 130 mm behind the shielding while the beam passes through the shielding material (Fig. 5b). In this case, the beam broadening is caused mainly by the interaction effects of the primary particles with the atoms in the much denser shielding material. While traversing a medium a charged particle undergoes many small-angle scatters and experiences Coulomb scattering from nuclei. The net multiple-scattering and displacement cause a beam broadening which are described by the Gaussian distribution. The Molière theory yields a detailed description of these effects [22]. Measurements of non-Gaussian tails typically indicate less-frequent hard scatter events. The width of the distribution is found to be inversely proportional to the momentum, velocity, and charge of incident particle. It is also proportional to the thickness of the scattering material [23,24]. The path of electrons is found from the analysis of the

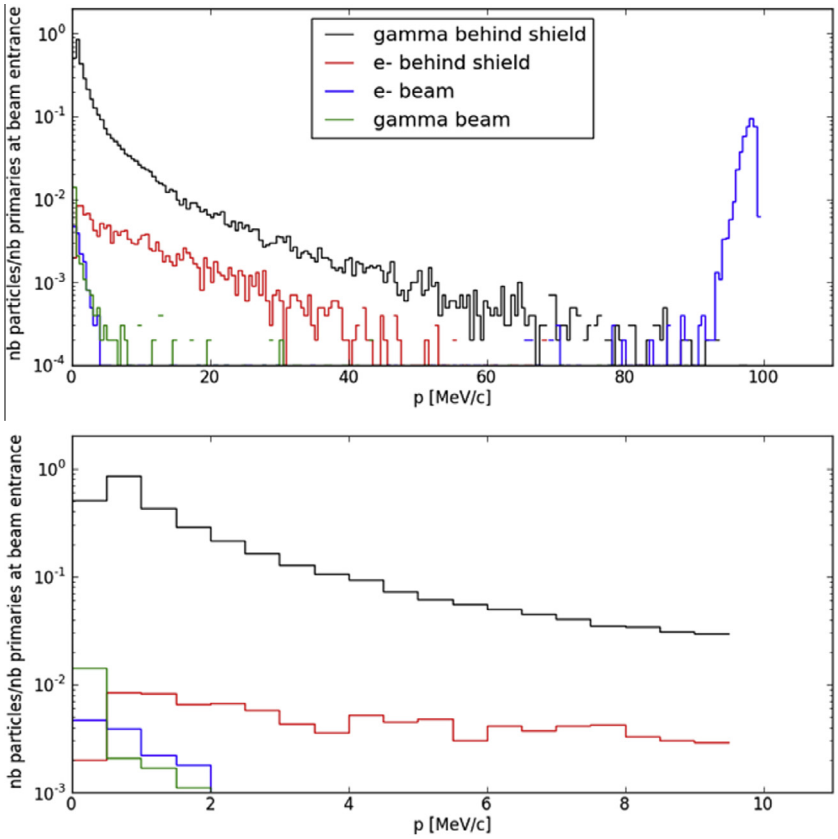

Fig. 3. Primary and secondary spectra of particles for the primary beam momentum of 100 MeV/c. The spectrum shown in blue is accompanied by very small fraction of primary gamma ray contamination (green). Secondary gamma rays (shown in black) measured behind the shield are the most dominant particle fraction. (For interpretation of the references to colour in this figure legend, the reader is referred to the web version of this article.)

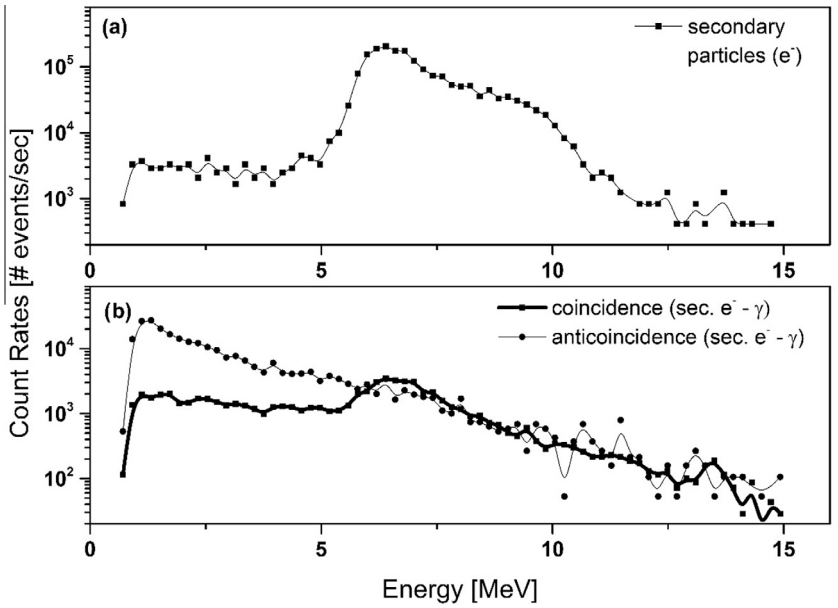

Fig. 4. (a) Energy spectrum of electrons produced by primary electron beam with momentum equal to 115 MeV/c as measured in the E-detector of the telescope. (b) The coincidence and anticoincidence spectra of secondary particles and γ-rays behind the shield.

beam profile to deviate from the straight line by 12.5° to 2.5° for the beam momentum 57.5 and 345 MeV/c, respectively (Fig. 5). Note that for beam momentum larger than 100 MeV the beam in addition to e^- contains also μ^- and π^-.

The secondary beam fluxes (including transmitted primaries if present) in the range of the applied beam momenta are presented in Fig. 5c. For the beam momenta lower than 57.5 MeV/c, the secondary beam flux was too low to be detected and can be derived

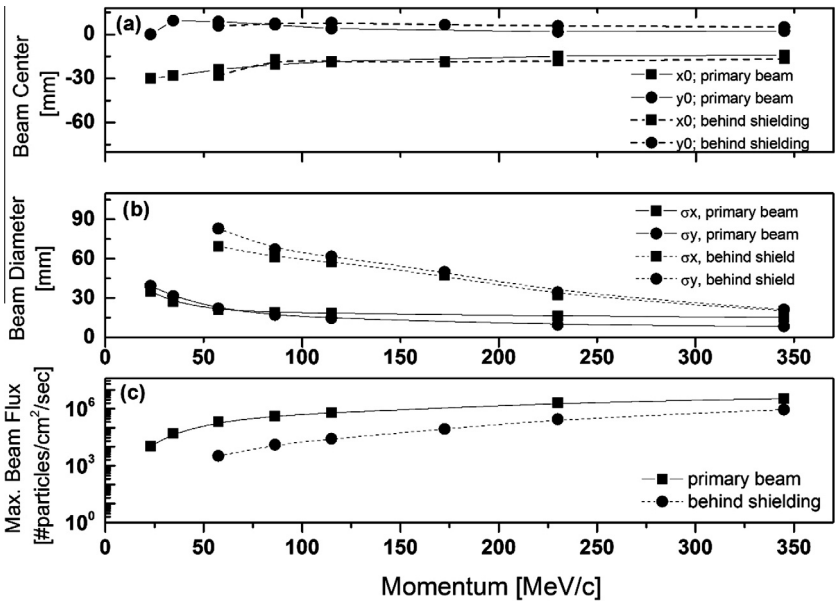

Fig. 5. Characteristics of the particle beam including central position (a), the beam spread from Gaussian fit (b), and the beam flux at the centre (c) measured at beam focal plane. The measurements with the radiation shielding were conducted 130 mm away from the focal plane after insertion of the radiation shielding at the beam focal plane location.

only by the extrapolation methods from the data obtained for larger beam momenta.

The experimental beam calibration studies were accompanied by the semi-quantitative modelling investigations of the interaction of the primary beam with the shielding. They were conducted to provide an understanding of the global properties of the experimental setup (Fig. 6). A simplified version of the detector system was implemented in the simulations. A large thin cylinder located behind the shielding was used to simplify the computing process. The beamline ion optics with traces representing the transport of particles into the measurement area are shown in Fig. 6. The analysis is performed by Monte Carlo simulation using GEANT4 equipped with the G4BL packet. The modelling tools allow also the generation and tracing of the secondary particles produced by the interaction of the incident beam with the surrounding materials. The analysis of the beam transmission through the current setup shows that a small fraction of synchrotron γ-rays (green rays, Fig. 6) can be produced while the beam passes through the last bending magnet. The beam focal plane and beam geometry derived from the modelling are found to agree with the results of the beam diagnostic measurements. The modelling studies after insertion of the shielding indicate a large production of γ-rays in the shielding. These studies also show that the angular spread of the generated γ-rays is much larger than the straggling of primary electrons (Fig. 6). More advanced, quantitative analyses of the interaction of primary particles with the shielding were performed for the measurements with the MCP detector in Section 3.3.

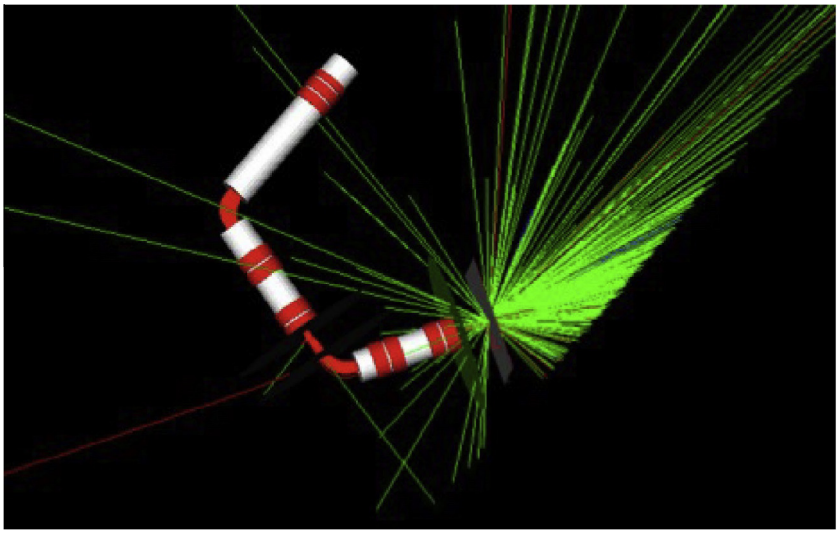

Fig. 6. Beam line model with transport of electrons in the PiM1 test area. Large purple circle shows beam pipe exit and entrance windows. Quadrupole magnets are represented as red cylinders. Green rectangular plate represent the radiation shielding used in the present experiments. Electron trajectories are showed as red and γ-rays as green colour curves. Modelling results of the interaction of primary electrons with Al–Ta–Al shielding for γ-rays (green traces) are angularly more spread than electrons. (For interpretation of the references to colour in this figure legend, the reader is referred to the web version of this article.)

3.2. MCP measurements of the radiation environment behind the shielding

3.2.1. MCP measurements and MCP particle rates

Fig. 7 shows an example of MCP measurements of the signals produced by the particle beam with the beam momentum of 115 MeV/c while passing the Al/Ta/Al shielding. The MCP detector was inserted ~32 mm behind the rear surface of the shielding assembly (Fig. 2b). The MCP normal was arranged collinearly with the beam axis. The incident beam crosses the shielding at 0° to the plane normal axis. The uppermost panel a in Fig. 7 shows all measured MCP waveforms with the pulse amplitudes $|V| = 2.5$ mV. Smaller amplitudes have contributions from electrical noise [19]. The panels b and c of Fig. 7 display an averaged MCP pulse amplitude and power spectrum, respectively, and this information is used for the diagnostic purposes.

Simultaneously with the MCP measurements, 50 MHz ($T = 20$ ns) synchrocyclotron waveforms are collected (Fig. 7, panel e). The MCP signals are separated according to their time-of-arrival at the detector with respect to synchrocyclotron waveform. Three well-separated groups of MCP pulses can be identified in the histogram for the beam momenta larger than 115 MeV/c and be assigned to electrons, muons, and pions. Because the distance from the shielding to the MCP detector is relatively small (~32 mm), there is practically no measurable time delay between the transmitted primary and the produced secondary particles. Therefore, each of the measured group of pulses contains both the primary (if present) and the secondary particles registered by the detector [21]. Because the MCP measurements cannot distinguish between various particles, the beam diagnostic measurements and modelling studies are employed to determine particle fractions for each of the secondary particle beams.

The temporal distribution of the signals within each group in the histogram can be fitted with a Gauss distribution (Fig. 7, panel e). For the pulse (charge) height distribution analysis all pulses within ±3 σ temporal range were analysed. The signals measured at other times were ascribed to the background radiation (scattering of secondary radiation from the structure, cosmic rays, environmental radiation). The dependence of the background radiation as a function of beam momentum is considered in Fig. 9.

Particle rates at the detector are determined from the charge distribution which were fitted well to negative exponent [19]. The calculation of the actual particle rate measured by the MCP detector is derived from the analysis of the charge distributions for each of the groups of pulses in the histogram. Fig. 8 shows the example of the pulse height and charge height distributions derived from the measurements of the radiation field produced by the incident beam with the momentum of 115 MeV/c. Here log-representation is chosen and a linear fit to the experimental data. Following the fit, the extrapolation to low amplitude/charge

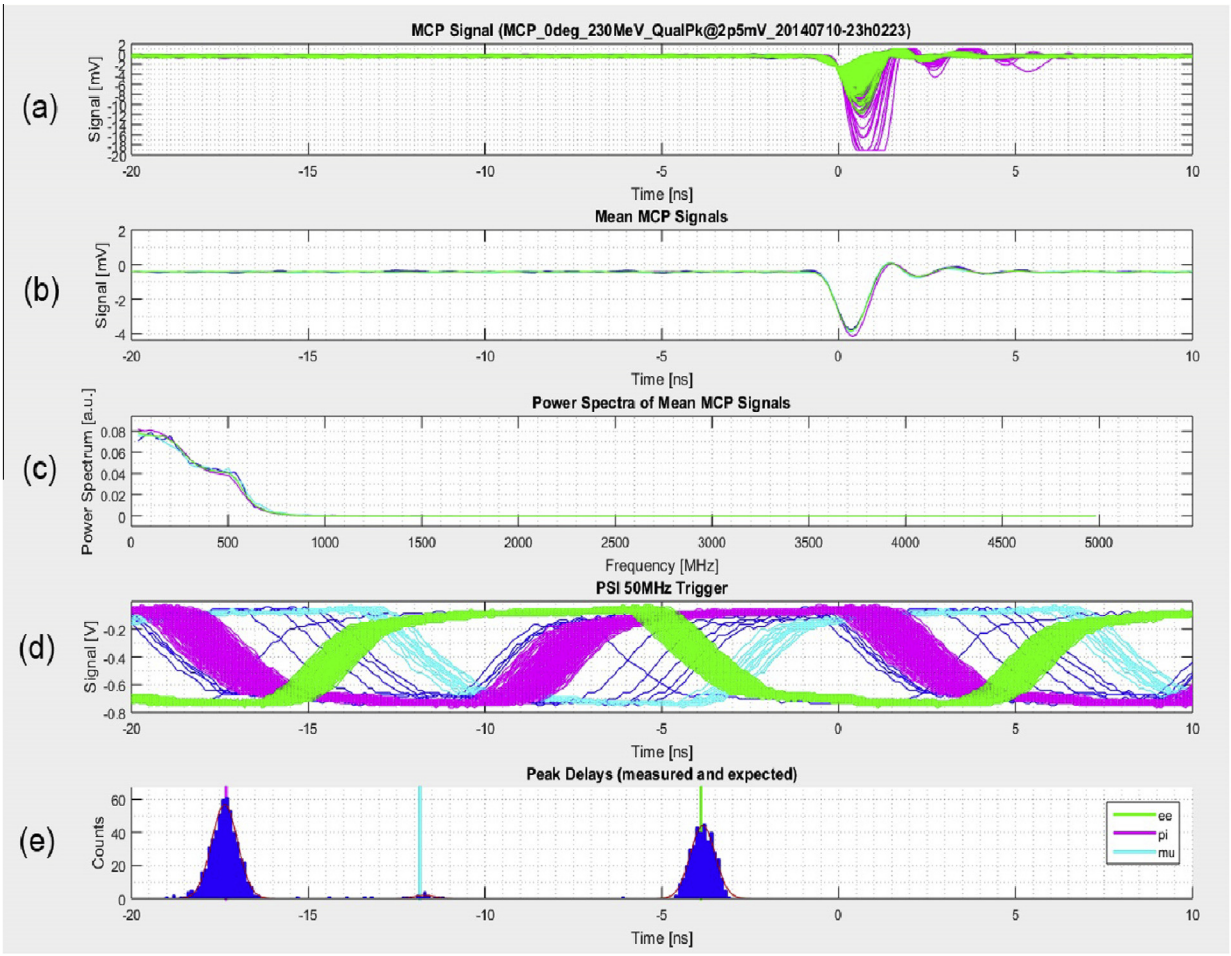

Fig. 7. Typical data set obtained for the MCP measurements of the radiation field generated by the interaction of primary e^-, μ^- and π^- beams with the radiation shielding material. (a) waveforms with the MCP pulses; (b) the mean MCP pulse signal; (c) the power spectrum of the MCP signals; (d) all synchrocyclotron waveforms recorded simultaneously with the MCP measurement; (e) the groups of pulses at times of arrival of incident e^-, μ^- and π^- beams obtained by synchronisation of measured pulses with the phase of synchrocyclotron.

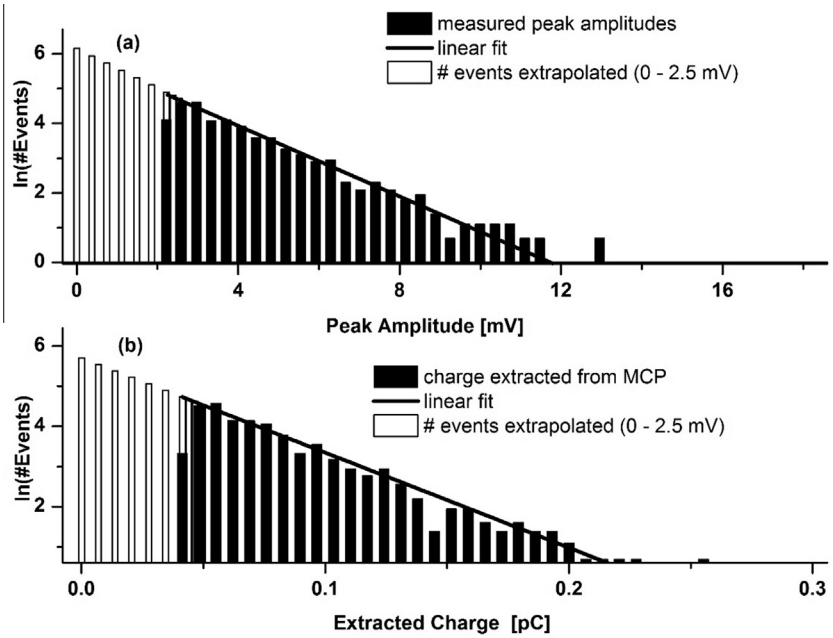

Fig. 8. Typical pulse (top panel) and charge height (bottom panel) distributions determined from the measurements of secondary radiation, which was produced by the interaction of the primary electron beam (beam momentum of 115 MeV/c) with the shielding. The black bars represent the results obtained in the measurements. For peak amplitudes smaller than $|V| = 2.5$ mV, the number of events were derived from linear extrapolation.

values can be made to derive finally the particle rate measured by the MCP detector. The analysis procedure is discussed in more detail, in our recent publication [19].

The primary particle rates expected at the active MCP detector surface area and the MCP detection rates for all secondary particles produced by the primary particles are presented in Fig. 9. The MCP particle rates determined from the charge distribution are plotted as background radiation since they do not correlate with the times-of-arrival of the primary e^-, μ^- and π^-. The rate of these uncorrelated events increases with the beam momentum and overall increase of the beam flux. Similar MCP background radiation rates were measured in the experiment without shielding and are likely caused by the interaction of secondary particles with the surrounding materials [19].

3.2.2. Transmission coefficients and MCP detection efficiencies at 0° incidence angle

Using the radiation shield, the MCP detection efficiencies to the radiation field produced by primary e^- and π^- as a function of beam momentum are presented in Fig. 10a and b, respectively. The effective MCP detection efficiency to secondary particles caused by incident e^- beam increases nearly linearly with the

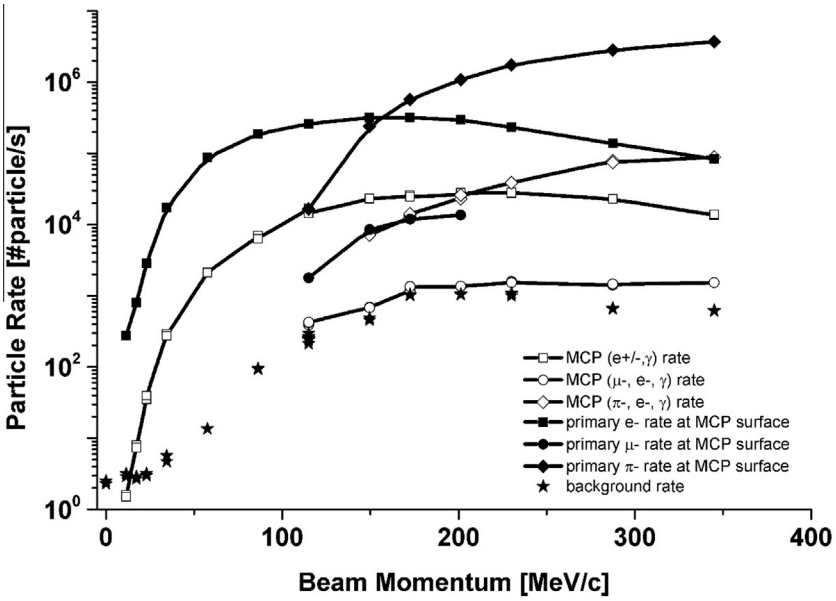

Fig. 9. Primary (incident) particle rates expected at the front MCP surface and particle rates measured by the MCP detector that are produced by primary (incident) particles in the function of the beam momentum. Background count rates are the particle rates of all uncorrelated events. Primary μ^- fluxes were determined only up to 200 MeV/c by diagnostic methods whereas the MCP rates were measured up to 345.5 MeV/c.

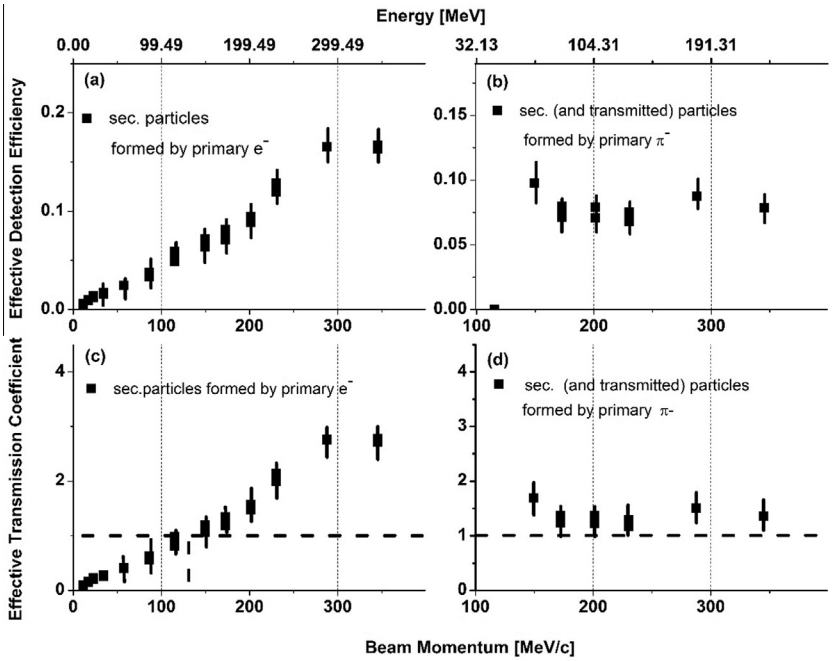

Fig. 10. The effective MCP detection efficiencies and effective transmission coefficients to radiation environment generated by the primary particles e^- (a) and (c), respectively and π^- (b) and (d), respectively. The error bars represent deviation from the mean values derived from 4 to 5 measurements at each applied beam momentum. In panels (c) and (d), the attenuation coefficients derived from modelling studies (Section 3.3) are plotted for the comparison with the experimental data.

increase of beam energy. For the lowest beam momentum the effective detection efficiency is 0.005 (±0.003) and rises to about 0.15 (±0.04) for the largest applied beam momentum (345 MeV/c). In contrast, the effective MCP detection efficiency to secondary radiation produced by the π^- is observed to be relatively constant in the range of applied beam momenta and is close to ~0.07 (±0,025) (Fig. 10b).

The effective MCP detection efficiency shown in Fig. 10a and b is the combined detection efficiency to all particles present behind the radiation shielding, including transmitted primaries and the various secondary particles. In case of an incident electron beam the secondary beam can contain e^+, e^-, and bremsstrahlung of various energies. For incident π^-, the secondary particle flux behind the radiation shielding consists mainly of transmitted primary and secondary π^- and e^- of various energies. The transmission values are derived as defined by Eq. (2). The MCP incident beam rate was calculated using the MCP detection efficiencies to primary e^- of 5.8% and for π^- of 6.0% in the applied momenta range [18,19]. Fig. 10c and d display the transmission of the radiation shielding for primary e^- and π^- beams separately, as a function of beam momentum.

For the beam momenta lower than 130 MeV/c, the radiation shielding material attenuates the incident electron beam. However, for larger beam momenta the transmission values become larger than 1 because of the secondary radiation produced in the radiation shielding, mostly the γ-rays. For the incident π^- beam, the effective transmission of the radiation shielding is close to 1 within the applied beam momentum range.

Our results indicate that the applied shielding is efficient for the attenuation of high-energy electrons for beam momenta lower than 130 MeV/c. The beam transmission increases quasi-linearly with the beam energy. An increase of γ-ray production with an increase of the beam momentum is likely responsible for the apparent increase of the shielding transmission. This conclusion is in a good agreement with the beam diagnostic studies that indicated γ fluxes almost 100 times larger than the e^- fluxes behind the radiation shielding (see Fig. 3). For the incident π^- the applied radiation shielding was relatively inefficient and the shielding effect is only achieved due to a low detection efficiency to secondary particles.

The radiation lengths of the shielding materials applied in this study are 166.9 and 5.4 g cm^{-2} for Ta and Al, respectively. The density of Ta allows to reduce significantly the flux of e^- in the investigated beam momentum range. Further, for even lower beam momenta the e^- transmission is expected to decrease to negligible level. Since 10 mm of Ta have a radiation length of 16.7 g cm^{-2}, 60 MeV electrons can be fully stopped by the radiation shielding [25]. The electron energy-loss depends on the value of the critical energy, E_c, which is defined as the energy at which bremsstrahlung rate is equal to the ionisation-loss rate. For Ta and Al materials, this energy is close to ~8 and ~47 MeV, respectively. At energies well below the critical energies, excitation and ionisation processes dominate. Within the incident electron energy range applied in this study, the energy-loss by radiation, bremsstrahlung, is the main energy-loss channel and is accompanied by the production of secondary e^- and e^+. The electrons lose their energy by bremsstrahlung nearly exponentially with travelling distance through the material. For energies larger than 1 MeV Bremsstrahlung photons begin to produce e^-/e^+ pairs at some 9/7 X_0 distance, where X_0 [g cm^{-2}] is radiation length. Radiation length is a measure of characteristic amount of matter traversed for these related interactions [23]. For increasingly larger electron energies, both, e^- and γ photons can contribute to e^-/e^+ shower production. The shower development leads to a lower average energy per electron and eventually also the photon energy becomes too low to continue this process and the shower cascade ends. For photons with energies lower than 1 MeV, either Compton scattering or photoelectric effect can occur. The latter process occurs in the keV energy range and can contribute to the production of low energy electrons.

In the beam momentum range, the μ^- and π^- particles are losing energy mainly through electromagnetic interaction with bound electrons either via excitation or ionisation processes [23].

Ionisation becomes a dominant process at the energies exceeding atomic binding energies. For both μ^- and π^- particles the ionisation efficiency become minimal for beam momenta in the range 200–300 MeV/c [23]. Below this minimum, the energy-loss is inversely proportional to particle velocity. Once the particle starts to slow down in the material its energy-loss will increase until it reaches the speed of electrons in the atoms. Then, the energy-loss starts to decrease for particle energies lower than 1 MeV. The energy-loss above the ionisation minimum increases slowly and is comparable for all materials. Hence, for μ^- and π^- in the momenta range applied in the present studies, the excitation processes including energetic knock-on electrons can be important in the energy-loss and occur typically in single collisions [26][27]. The collisional energy-losses are well described by Bethe-Bloch theory [28]. They are proportional to the electron density in the material, atomic number Z, and inversely proportional to the speed of the incident particle. The specific energy-loss of particles is a function of its momentum and is proportional to the number of electrons (Z) in the material and square of the particle charge. For μ^- and π^- the energy-loss by radiation is relatively unimportant in the range of energies applied in the current studies. In high Z materials, the critical energy, E_c is reached at several hundreds of GeV [29–31].

3.2.3. MCP particle rates and detection efficiency in the range of 0–180°

The MCP particle rates and the effective MCP detection efficiencies to radiation environment produced by incident e^- and π^- beams were investigated at various angles of the MCP surface with respect to the direction of incident primary particle beam (see Fig. 3b for the mechanism of MCP rotation). The MCP particle rates for both incident e^- and π^- beams are plotted in Fig. 11a and b, respectively. The rates determined from this study decrease with an increase of the angle in the range of angles 0° to ±90°. The MCP particle rates are largest for 0° and 180° and smallest (by about 20%) at the MCP angles −90° and +90° for the beam momenta larger than 75 MeV/c. To determine the effective MCP detection efficiency, the primary particle rates were derived at the effective MCP surface exposed to the direction of the incident particles. Because the surface area changes as the *cosine* function of the MCP angle, the effective MCP incident particle rate is expected to decrease with the increase of the angle in the angle range 0° to ±90°. At ±90° the cross-sectional area of the MCP plate is applied ($8 \times 0.6\ mm^2$). The effective MCP detection efficiency determined at the various MCP angles for incident e^- and π^- beams are plotted in Fig. 11c and d, respectively.

An increase of the effective detection efficiency with an increase of the MCP angle indicates that in spite of the reduced incident particle rate, the MCP secondary particle rate does not decrease accordingly. This can occur either due to an increase of secondary particle rate and/or increase of the MCP detector sensitivity to radiation environment. With an increase of the MCP angle, also the effective MCP thickness increases as the function of *sine* of the MCP angle; the MCP thickness rises from 0.6 mm at 0° to 8 mm at ±90°. Hence, the cross-sectional particle incidence area is enlarged resulting in a larger probability of particle interaction with the MCP. For 0° and 180° incident angles, the effective thickness of MCP is 1.2 mm (thickness of two MCP plates) and for 90 and −90°, the effective thickness increases to several mm (MCP diameter is 8 mm), which can result in an increase of the MCP detection efficiency. By increasing the MCP thickness the detection of γ-rays or e^- also increases [32–34]. The analysis of these angle-dependant effects requires more detailed modelling and experimental studies.

3.3. Modelling studies of particle interaction with shielding: MCP setup

Detailed modelling studies of the interaction of high-energy (e^-, μ^-, π^-) beams with Al (1 mm)–Ta (10 mm)–Al (1 mm) sandwich and materials of the experimental setup (Figs. 2b and 12) were conducted by GEANT4/GRAS modelling tools [35,36]. GEANT4 includes processes for tracking of particles in 3D volumes. The software also includes a suite of physics models that deals with particle interaction with matter. GRAS is an application that contains

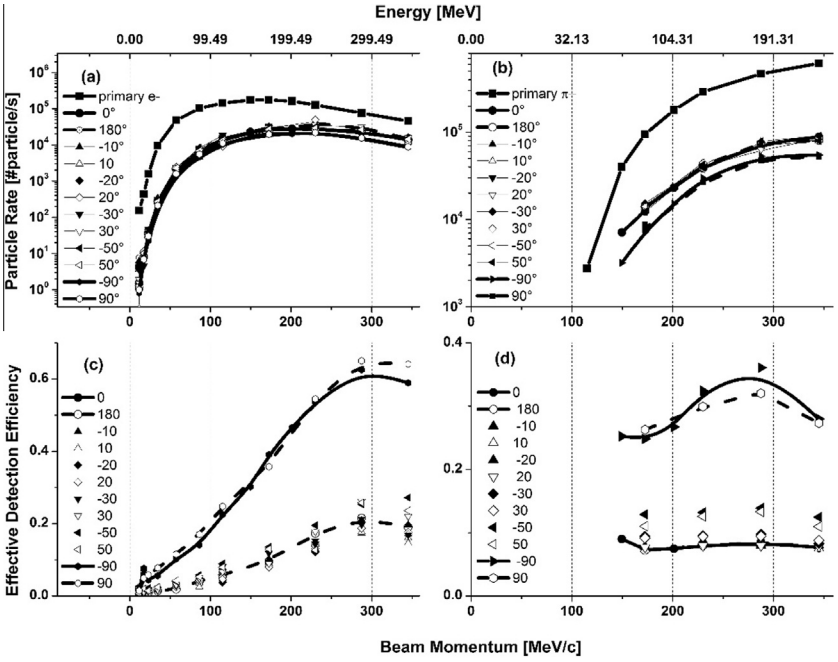

Fig. 11. MCP particle rates (a) and (b) and effective detection efficiencies to the secondary beam produced by e^- (c) and π^- (d), respectively, for various incident angles and beam momenta. The MCP particle rates decrease more slowly than the effective primary particle rates with the increase of angle. Hence, the effective detection efficiency is observed to increase with the angle increase.

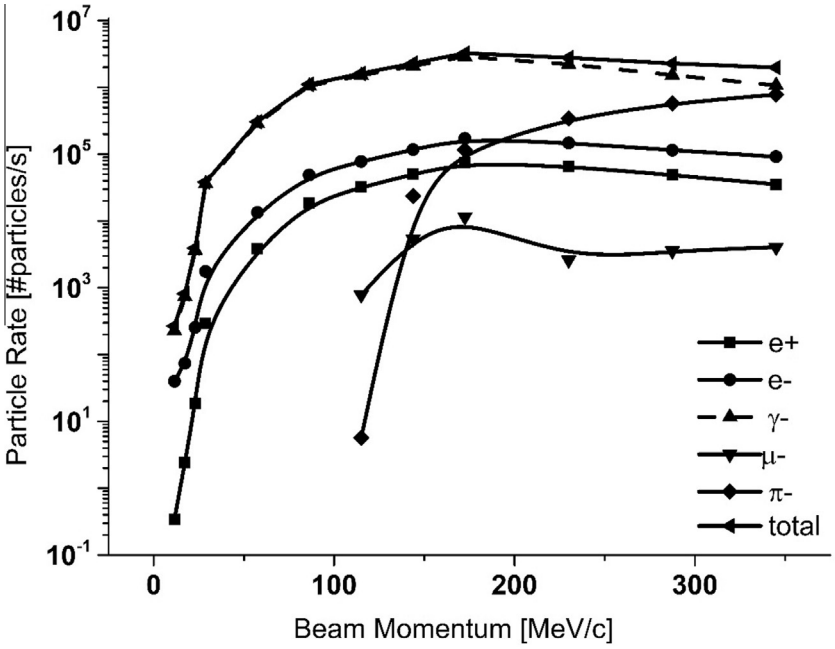

Fig. 12. Secondary particle rate derived from the modelling studies at the front MCP surface positioned with the active surface perpendicular to the beam direction. Data are given in Table 6.

different common analysis modules. These modules support the definition of parameter, data generation and extraction of appropriate data in GEANT4. This means that the GRAS user does not need to write dedicated software to make use of GEANT4 processes and models.

The physical models include standard electromagnetic model for analysis of ionisation, bremsstrahlung, Compton scattering, photoelectric effect, and the QGSP_BERT_HP setup for hadronic interactions such as elastic or inelastic scattering. GEANT4 has long heritage in the high-energy community and has typical accuracy better than 5%. The accuracy of the modelling results depends on details of analysed geometry and the settings of parameters such as production cuts. This typically defines the limits of secondary production and thereby also the resolution of the simulation. The production cut for the present modelling work was set to 0.01 mm, well within the needed resolution.

The geometry for this work is based on the 3D mechanical models of the real experimental setup [19]. Instead of detailed detector assembly, a vacuum target sphere was placed in the location of the MCP detector to calculate particle fluxes. The primary beams for the simulations were constructed using the beam calibration data (beam fluxes, beam geometrical parameters and particle fractions).

In the calculation, a mixed beam was applied for direct comparison with the results of diagnostic methods. Tables 2 and 3 shows the results of the calculation of particle fluxes and fractions of total flux and of secondary particle flux. The μ^- and π^- particles are present in the secondary beam for the beam momenta larger than 115 MeV/c. The calculated beam fraction of total flux never exceeds 0.2–0.4%; the pion fraction rises to ~40% at the maximal beam momentum applied in this study. The secondary μ^- and π^- fractions are found to be smaller than 1% of the total fraction of secondary particles. At lowest beam momenta, the electron fraction of total flux reaches ~15% and production of γ-rays decreases to 85% (Table 2). The e^+ fractions of secondary products increases with an increase of the beam momentum from 0.1% for the lowest beam momentum to ~3% for the largest beam momentum. The fraction of secondary e^- is calculated to be 3%. It is found also relatively constant in the applied beam momentum range. Only for

Table 2
GRAS/GEANT4 calculated particles fluxes and fractions of different species at the MCP location from the incident primary particles (e^-, μ^- and π^-). The fractions of the incident beam, total flux and beam intensity determined in the diagnostic studies are used in calculations as the input parameters.

Beam momentum [MeV/c]	Total flux at MCP location [#particle/s*cm^2]	Fraction of total flux at MCP location [%]				
		e^+	e^-	γ	μ^-	π^-
11.5	5.34E+02	0.1	14.8	85.1	0.0	0.0
17.25	1.62E+03	0.3	9.1	90.6	0.0	0.0
23	7.81E+03	0.5	6.5	93.0	0.0	0.0
28.75	7.62E+04	0.8	4.6	94.6	0.0	0.0
57.5	6.06E+05	1.3	4.4	94.4	0.0	0.0
86.25	2.22E+06	1.7	4.4	94.0	0.0	0.0
115	3.23E+06	2.0	4.8	93.2	0.0	0.0
143.75	4.57E+06	2.2	5.1	91.5	0.2	1.0
172.5	6.47E+06	2.3	5.3	88.5	0.4	3.6
230	5.53E+06	2.4	5.3	79.8	0.1	12.4
287.5	4.53E+06	2.1	5.0	67.4	0.2	25.3
345	3.95E+06	1.8	4.6	53.9	0.2	39.5

Table 3
GRAS/GEANT4 calculations of total flux of secondary products and their fractions at MCP location. The flux of secondary products are derived using the results of diagnostic studies as the input parameters.

Beam momentum [MeV/c]	Flux of secondary products [particle/s*cm^2]	Fraction of secondary products at MCP location [%]				
		e^+	e^-	γ	μ^-	π^-
11.5	4.77E+02	0.1	4.5	95.3	0.0	0.0
17.25	1.53E+03	0.3	3.7	96.0	0.0	0.0
23	7.55E+03	0.5	3.3	96.2	0.0	0.0
28.75	7.50E+04	0.8	3.0	96.2	0.0	0.0
57.5	5.98E+05	1.3	3.1	95.6	0.0	0.0
86.25	2.19E+06	1.7	3.2	95.1	0.0	0.0
115	3.18E+06	2.0	3.4	94.6	0.0	0.0
143.75	4.44E+06	2.2	3.7	94.1	0.0	0.0
172.5	6.11E+06	2.4	3.9	93.6	0.0	0.0
230	4.76E+06	2.8	4.4	92.7	0.1	0.1
287.5	3.33E+06	2.9	5.1	91.6	0.2	0.2
345	2.36E+06	3.0	6.1	90.2	0.3	0.4

the lowest and largest beam momenta this value increases to 5–6%. The e^+ beam fraction of the secondary particle flux is observed to rise gradually with the increase of the beam momentum from 0.1 to 3% whereas the electron fraction remains close to 3%. Only for the lowest and highest beam momenta, electron fractions are larger and close to 4% and 5–6%, respectively. The γ-ray flux fraction is the largest (∼90%) in the applied beam momenta range. The γ-ray fraction correlates well with the changes of the incident e^- fractions and increases gradually with the increase of the beam momentum. Tables 2 and 3 shows the results of the calculation of particle fluxes and fractions of total flux and of secondary particle flux.

The secondary products that reach the target sphere have their origin mainly from the shielding. Nevertheless, also secondary particles originating from the rear window contribute to the flux at the MCP location. This fraction of the total flux decreases from about 17% for lowest beam momenta to about 5% for the largest beam momentum (Table 4). The calculations show that for the lowest beam momenta, up to 11% of the primary electrons pass through the shielding. This value decreases to 1% for the beam momentum of 115 MeV/c. For larger beam momenta fraction of primary μ^- and π^- start to increase. The fraction of secondary products is larger than 90% for the beam momenta lower than 230 MeV/c. Above 230 MeV/c, the fractions of primary pions start to increase and reach value of ∼41% for the largest applied beam momentum (Table 4). Electron fraction of secondary products by means of primary particles is the largest in the entire range of the applied beam momentum (Table 5).

Table 5 shows that the electron fraction of the flux of the secondary products dominates considering the primary beams for all investigated beam momenta. The contribution from the π^- particles rise steadily with the beam momentum. The fraction of μ^- is practically negligible. The fraction of secondary e^- decreases, mainly due to increase the π^- fraction.

The modelling results agree well with the measurements results by diagnostic methods (Figs. 4 and 14). The diagnostic methods indicated large production of γ-rays dominating the fractions of all secondary particles. The calculations and beam diagnostic measurements show that the γ photon fraction is close to 95% and form the largest fraction of the radiation effects produced by the shielding. The secondary electrons and positrons contribute only a few percent of the total beam flux behind the shielding. The modelling studies indicate also that the fluxes of γ-rays increases with the beam momentum with the rate larger than secondary electron rate.

Table 4
GRAS/Geant4 calculation of the total flux at MCP, fraction of transmitted primary, secondary and secondary origin from rear. The latter are produced by the interaction of primary particles with surrounding materials, mostly behind the MCP detector.

Beam momentum [MeV/c]	Total flux at MCP location [#particles/s*cm^2]	Fraction of transmitted primaries	Fraction of secondary products	Fraction of secondaries originated from rear window
11.5	5.34E+02	10.8%	89.2%	17.1%
17.25	1.62E+03	5.6%	94.4%	13.3%
23	7.81E+03	3.3%	96.7%	11.3%
28.75	7.62E+04	1.6%	98.4%	8.7%
57.5	6.06E+05	1.3%	98.7%	6.6%
86.25	2.22E+06	1.2%	98.8%	5.1%
115	3.23E+06	1.5%	98.5%	4.8%
143.75	4.57E+06	2.8%	97.2%	4.8%
172.5	6.47E+06	5.5%	94.5%	4.3%
230	5.53E+06	13.8%	86.2%	4.3%
287.5	4.53E+06	26.4%	73.6%	4.4%
345	3.95E+06	40.3%	59.7%	4.5%

Table 5
GRAS/Geant4 calculations of the flux of secondary products and fraction of secondary products by primary particles.

Beam momentum [MeV/c]	Flux of secondary products [particle/s*cm^2]	Fraction of secondary products by primaries [%]		
		e^-	μ^-	π^-
11.5	4.77E+02	100	0	0
17.25	1.53E+03	100	0	0
23	7.55E+03	100	0	0
28.75	7.50E+04	100	0	0
57.5	5.98E+05	100	0	0
86.25	2.19E+06	100	0	0
115	3.18E+06	99.7	0.1	0.2
143.75	4.44E+06	99.2	0.0	0.8
172.5	6.11E+06	99.0	0.0	1.0
230	4.76E+06	97.0	0	3.0
287.5	3.33E+06	93.4	0	6.6
345	2.36E+06	88.4	0	11.6

Table 6 delivers a summary of particle rate at MCP surface at 0° angle to the direction of incident primary beam and Fig. 12 displays the particle fluxes as a function of the beam momentum expected at the MCP front plate.

For the direct comparison with the MCP results, the fluxes of secondary products produced either by incident e^- or π^- particles were calculated. The results of these calculations are shown in Fig. 13. For e^- incident beam, γ-flux is observed to increase readily with the increase of the beam momentum. It becomes larger than the incident e-flux for the momenta larger than 50 MeV/c. Also secondary e^- and e^+ flux increases with the increase of the beam momentum, but with lower rate. The fluxes of primary and secondary e^- become comparable for the beam momenta ∼350 MeV/c. For the incident π^-, secondary π^- are the largest fraction of the radiation environment behind the radiation shielding. Other particles, γ-rays, e^-, e^+ and transmitted primary π^- form small fraction of the total flux of the secondary radiation. The rate of secondary particle flux increase is observed to be similar with the rate of increase of the primary π^-.

The modelling studies provide means for the direct comparison with the MCP experiment. In the following, we compare the effective beam transmission coefficients T (P_i) of the shielding to the incident e^- and π^- beams, respectively, as defined by the Eq. (2) (Section 2.4). The particle rates determined in the modelling studies have to be reduced to the MCP particle rates by applying the detection efficiency of the MCP detector to relevant particles. To derive the MCP-relevant particle rates, the modelling results for the individual primary and secondary particles are multiplied by MCP detection efficiencies to these particles. Because the MCP detection efficiency to γ-rays was not investigated yet by our detector, we apply the value of this coefficient from the literature reports as ∼2% [34,37,38]. For the calculation of the incident e^- and π^-, respectively, their detection efficiencies published recently were used [19]. In the calculation of the MCP secondary e^- rates, the MCP detection efficiency of 16% was used, assuming that the largest fraction of the secondary e^- will have energies in sub-MeV energy range [18,19,39]. Fig. 14 compares both the modelling and experimental attenuation coefficient curves. For the incident e- beam the correlation is better if the MCP detection efficiency to γ photons is close to 1% rather than to 2% with the γ-rays dominating the flux at the MCP detector based on the GEANT4 calculations. Note that the energy distribution of secondary e^- and e^+ is unknown, introducing an uncertainty in this analysis. The effective transmission coefficients obtained from analysing modelling data of the secondary particles produced by incident π^- beam are close

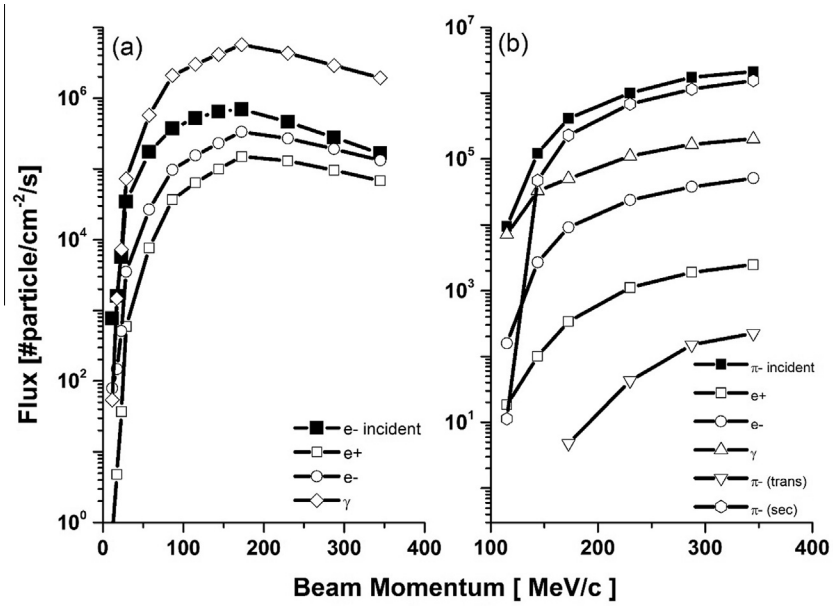

Fig. 13. Comparison between fluxes of the incident e^- (a) and π^- (b) and secondary particle beams derived from the modelling studies. For incident e^- beam the flux of g-rays increases readily with increase of the beam momentum. For incident π^-, the flux of secondary π^- is the largest.

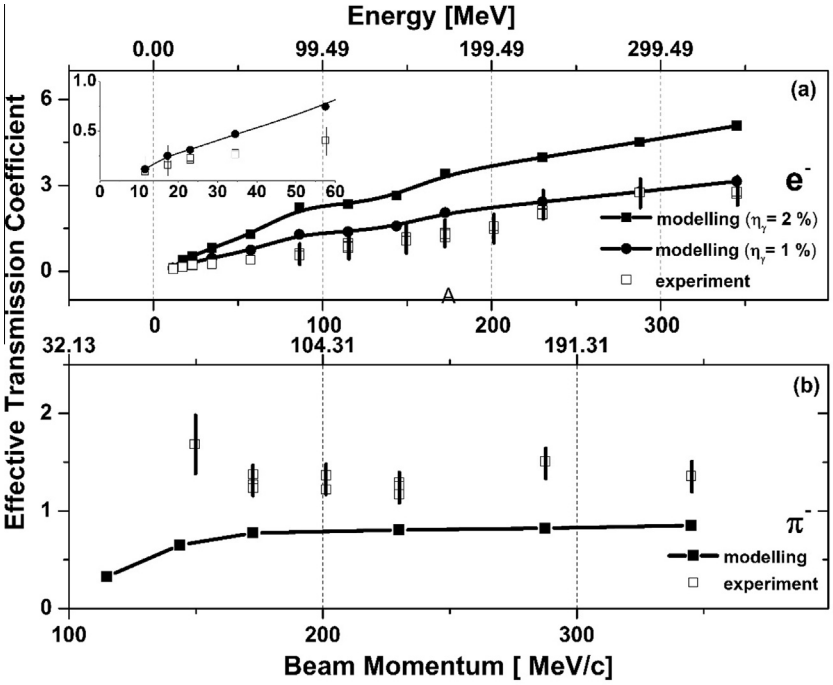

Fig. 14. Comparison between the effective transmission coefficients determined experimentally and derived from the modelling analysis. The results obtained by modelling and measured by the MCP detector are found to be close to each other for the analysis of incidence e^- (upper panel). More detailed comparison between the modelling and experiment in low energy region is shown in the graph inserted in panel a. The analysis of both results for incident π^- beam yield a discrepancy of about 30% between the calculated and measured values of the effective transmission coefficients (lower panel).

to one in the applied beam momentum range, which is about 30% too low compared to the experimental data.

3.4. Key performance indicators

The ratio determined from the integral of the MCP detection efficiency multiplied by the electron flux and the integral of the electron flux at the Europa moon over the important electron energy range from 20 keV–1 GeV is considered as the performance parameter proposed in modelling study [40]. Here, we calculate *the suppression ratio coefficient*, κ, for the flux of penetrating radiation taking into account our experimental data with their extrapolation to lower and higher energy ranges, and the electron flux adopted for the moon Europa:

$$\kappa = \frac{\int_{20keV}^{1GeV} f(E)_{Europa} \cdot \eta_{S/NS}(E) dE}{\int_{20keV}^{1GeV} f(E)_{Europa} dE} \quad (3)$$

Table 6
Particle rate at MCP positioned with active surface perpendicular to the beam direction (@0.5026 cm^2 cross-section (Ø 8 mm MCP).

Beam momentum [MeV/c]	Rate at MCP location [#particles/s]					
	e^+	e^-	γ	μ^-	π^-	Total
11.5	0.342	39.8	228	0	0	268
17.25	2.41	74.2	739	0	0	816
23	18.6	255.0	3650	0	0	3930
28.75	295	1760	36,200	0	0	38,300
57.5	3830	13,400	288,000	0	0	305,000
86.25	18,400	48,700	1,050,000	0	0	1,110,000
115	32,000	77,900	1,510,000	783	5.69	1,620,000
143.75	49,900	117,000	2,100,000	5380	23,700	2,300,000
172.5	74,900	172,000	2,880,000	11,500	116,000	3,250,000
230	65,800	147,000	2,220,000	2600	344,000	2,780,000
287.5	48,800	115,000	1,530,000	3570	576,000	2,280,000
345	35,300	91,600	1,070,000	4050	784,000	1,980,000

here $f(E)_{Europa}$ is the incident electron flux at the orbit close to Europa (differential flux at Europa 2: worst case radiation scenario) [41] and $\eta_{S/NS}$ is the effective detection efficiency of the MCP detector in the electron energy ranges within 20 keV–1 GeV as derived from the experiments. For the determination of the η coefficient for the entire energy range, a linear extrapolation is applied. Both the differential electron flux and a reduced electron flux due to the applied shielding expected at Europa in the function of electron energy are shown in Fig. 15. The numerical integration of these fluxes over the 20 keV–1 GeV energy range yields:

$$\kappa \approx 6.8 \cdot 10^{-3}$$

For the reduced energy range from 100 keV to 1 GeV this value is about 3% smaller. This value is larger by about factor of 5 compared with the earlier modelling results by Desorgher ($\kappa = 7{\cdot}10^{-4}$, $\eta\gamma = 6\%$) [40]. That theoretical analysis considered a radiation shielding similar to that applied in our investigations but only calculated the transmission of primary electrons and the generation of secondary γ-rays. The suppression coefficient value of $\leqslant 10^{-3}$ would be necessary to fulfill the scientific scope at Europa.

The experimental studies provide the attenuation of the radiation shielding to the incident high-energy electrons. Unfortunately, the high bremsstrahlung production that increases nearly linearly with the incident electron beam produces additional background radiation. Although the incident beam can be well attenuated for electron beam momenta lower than 130 MeV, above this value the shielding functions as the radiation environment amplifier. By combining present shielding with other materials attenuating the γ-rays further improvements of the shielding attenuation performance can be achieved. The scattering and absorption of γ-rays are related to the density and effective atomic numbers of the material, knowledge of the mass attenuation coefficients is of primary importance. High Z, high density composites including bismuth, uranium or tungsten can offer superior attenuation of γ-rays [42]. Other solutions to improve the reduction of secondary radiation behind the shielding would be tuning the (*structural* to be removed) geometrical parameters (pitch, length and diameter of the channels) of the MCPs [37] and their chemical composition as for example using lead-free material having a lower sensitivity to penetrating radiation [37].

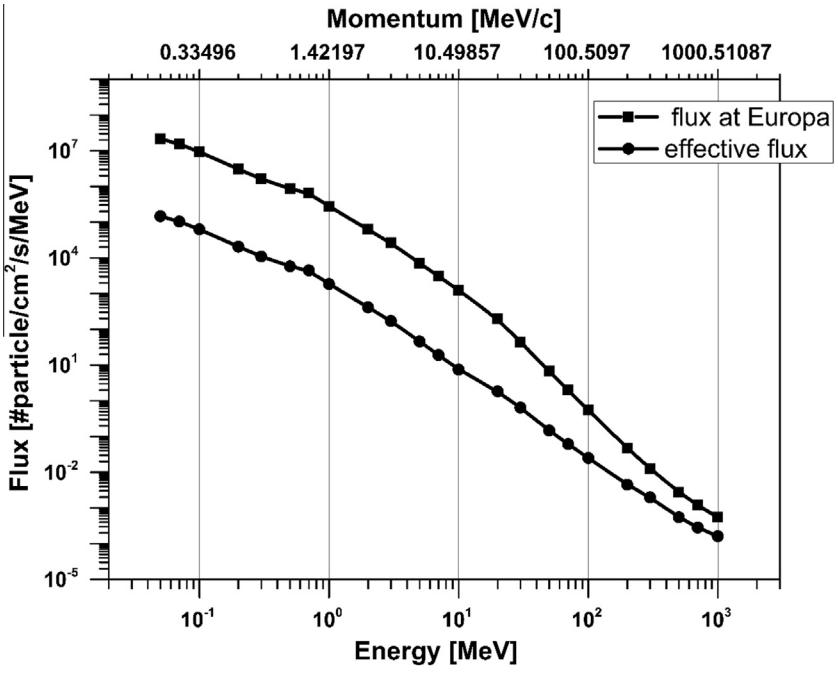

Fig. 15. Flux at Europa environment and the predicted at the MCP active surface area while applying Al/Ta/Al radiation shielding.

4. Conclusions

The experimental and modelling studies of the performance of Al/Ta/Al material as a radiation shielding of the incident electron beam were conducted in the momentum range 17–345 MeV using beam diagnostic methods and MCP detector designed for the NIM instrument on the JUICE mission. The studies provide the quantitative analysis of the effective MCP detection efficiency to the secondary particles and values of the effective transmission coefficients in the applied incident electron energy range. Although the selected shielding provides considerable attenuation of the high-energy electron beam, the produced secondary radiation by the interaction with the radiation shielding material reduces the initial attenuation effects. The largest fraction of the secondary radiation is bremsstrahlung, high-energy γ-rays whose production rate increases nearly linearly with the increase of the incident electron energy. At the electron energy close to 130 MeV the effective MCP particle rates of secondary radiation and incident electrons are equal and shielding does not attenuate the incident beam any more. For larger incident electron energies the shielding act as the amplifier of the incident electron beam; the secondary radiation rate become larger than that of the incident electron beam. Nevertheless, the effective detection efficiency is low and reaches about 0.17 (17%) for the maximal incident electron energy applied in this study. The effective particle flux is predicted at the moon Europa at its worse radiation scenario. The suppression coefficient determined as the ratio of the integrated values of the effective flux to flux expected at the Europa moon gives values about five times larger than that derived from earlier modelling studies. By introducing high Z material to attenuate γ-rays, further improvements of the shielding attenuation performance can be made. Other improvements are also possible by applying optimised MCP plate geometrical parameters (channel pitch, length and diameter) which are less sensitive to the secondary radiation. The experimental results confirm very well modelling predictions in the investigated electron energy range within uncertainties considering the MCP detection efficiency to γ-rays or possible contribution from the low energy secondary electron. Future studies of the MCP detection efficiency to γ-rays will clarify observed differences.

Acknowledgments

The authors would like to acknowledge the contribution of a number of people helping in technical preparation of the beamline setup for the presented investigations including construction engineers: Stefan Brüngger, Philippe Németh and mechanical workshop. The financial support from SNSF and Swiss Space Office is acknowledged.

References

[1] O. Grasset, M.K. Dougherty, A. Coustenis, E.J. Bunce, C. Erd, D. Titov, M. Blanc, A. Coates, P. Drossart, L.N. Fletcher, H. Hussmann, R. Jaumann, N. Krupp, J.P. Lebreton, O. Prieto-Ballesteros, P. Tortora, F. Tosi, T. Van Hoolst, JUpiter ICy moons Explorer (JUICE): an ESA mission to orbit Ganymede and to characterise the Jupiter system, Planet. Space Sci. 78 (2013) 1–21.
[2] P. Wurz, D. Abplanalp, M. Tulej, M. Iakovleva, V.A. Fernandes, A. Chumikov, G. G. Managadze, Mass spectrometric analysis in planetary science: investigation of the surface and the atmosphere, Sol. Syst. Res. 46 (2012) 408–422.
[3] P. Wurz, D. Abplanalp, M. Tulej, H. Lammer, A neutral gas mass spectrometer for the investigation of lunar volatiles, Planet. Space Sci. 74 (2012) 264–269.
[4] D. Abplanalp, P. Wurz, L. Huber, I. Leya, E. Kopp, U. Rohner, M. Wieser, L. Kalla, S. Barabash, A neutral gas mass spectrometer to measure the chemical composition of the stratosphere, Adv. Space Res. 44 (2009) 870–878.
[5] P. Wurz, L. Gubler, Fast microchannel plate detector for particles, Rev. Sci. Instr. 67 (1996) 1790–1793.
[6] A. Vorburger, P. Wurz, H. Lammer, S. Barabash, O. Mousis, Monte-Carlo simulation of Callisto's exosphere, Icarus 262 (2015) 14–29.
[7] J. TEAM, JUpiter ICy Moons Explorer Exploring the Emergence of Habitable Worlds around Gas Giants, JUICE RED BOOK, ESA, 2014, pp. 1–124.
[8] P. Wurz, H. Lammer, Monte-Carlo simulation of Mercury's exosphere, Icarus 164 (2003) 1–13.
[9] D.O. Kataria, Microchannel plates at high rates: the challenges for future space plasma missions, J. Vac. Sci. Technol. B 24 (2006) 1040–1044.
[10] K.P. Klaasen, M.J.S. Belton, H.H. Breneman, A.S. McEwen, M.E. Davies, R.J. Sullivan, C.R. Chapman, G. Neukum, C.M. Heffernan, Inflight performance characteristics, calibration, and utilization of the Galileo solid-state imaging camera, Opt. Eng. 36 (1997) 3001–3027.
[11] P.D. Fieseler, S.M. Ardalan, A.R. Frederickson, The radiation effects on Galileo spacecraft systems at Jupiter, IEEE Trans. Nucl. Sci. 49 (2002) 2739–2758.
[12] G.W. Fraser, A.D. Pearson, G.C. Smith, M. Lewis, M.A. Barstow, The gain characteristics of microchannel plates for X-ray photon counting, IEEE Trans. Nucl. Sci. 30 (1983) 455–560.
[13] M. Galanti, R. Gott, J.F. Renaud, High resolution, high sensitivity channel plate image intensifier for use in particle spectrographs, Rev. Sci. Instr. 42 (1971) 1819.
[14] G. Moldovan, J. Matheson, G. Derbyshire, A. Kirkland, Characterisation of a detector based on microchannel plates for electrons in the energy range 10–20 keV, Nucl. Instr. Meth. A 596 (2008) 402–408.
[15] D.K. Waterhouse, J.F. Williams, The performance of a microchannel-plate-based position sensitive detection system, Rev. Sci. Instr. 68 (1997) 3363–3370.
[16] J.P. Macau, J. Jamar, S. Gardier, Review of influence of radiations on channeltrons and channel plates, IEEE Trans. Nucl. Sci. 23 (1976) 2049–2055.
[17] M.I. Babenkov, V.S. Zhdanov, S.A. Starodubov, Chevron of microchannel plates as position-sensitive detector for beta-spectrometers, Nucl. Instr. Meth. A 252 (1986) 83–86.
[18] R.C. Blase, R.R. Benke, C.M. Cooke, K.S. Pickens, Microchannel plate detector detection efficiency to monoenergetic electrons between 0.4 and 2.6 MeV, IEEE Trans. Nucl. Sci. 62 (2015) 3339–3345.
[19] M. Tulej, S. Meyer, M. Luthi, D. Lasi, A. Galli, L. Desorgher, W. Hajdas, S. Karlsson, L. Kalla, P. Wurz, Detection efficiency of microchannel plates for e(−) and pi(−) in the momentum range from 17.5 to 345 MeV/c, Rev. Sci. Instr. 86 (2015).
[20] E.A. MacDonald, M.F. Thomsen, H.O. Funsten, Background in channel electron multiplier detectors due to penetrating radiation in space, IEEE Trans. Nucl. Sci. 53 (2006) 1593–1598.
[21] W. Hajdas, L. Desorgher, K. Deiters, D. Reggiani, T. Rauber, T.M.P. Wurz, L.M.K. Wojczuk, P. Kalaczynski, High energy electron radiation exposure facility at PSI, J. Appl. Math. Phys. 2 (2014) 910–917.
[22] H.A. Bethe, Moliere theory of multiple scattering, Phys. Rev. 89 (1953) 1256–1266.
[23] K.A. Olive, K. Agashe, C. Amsler, M. Antonelli, J.F. Arguin, D.M. Asner, H. Baer, H. R. Band, R.M. Barnett, T. Basaglia, C.W. Bauer, J.J. Beatty, V.I. Belousov, J. Beringer, G. Bernardi, S. Bethke, H. Bichsel, O. Biebel, E. Blucher, S. Blusk, G. Brooijmans, O. Buchmueller, V. Burkert, M.A. Bychkov, R.N. Cahn, M. Carena, A. Ceccucci, A. Cerri, D. Chakraborty, M.C. Chen, R.S. Chivukula, K. Copic, G. Cowan, O. Dahl, G. D'Ambrosio, T. Damour, D. de Florian, A. de Gouvea, T. DeGrand, P. de Jong, G. Dissertori, B.A. Dobrescu, M. Doser, M. Drees, H.K. Dreiner, D.A. Edwards, S. Eidelman, J. Erler, V.V. Ezhela, W. Fetscher, B.D. Fields, B. Foster, A. Freitas, T.K. Gaisser, H. Gallagher, L. Garren, H.J. Gerber, G. Gerbier, T. Gershon, T. Gherghetta, S. Golwala, M. Goodman, C. Grab, A.V. Gritsan, C. Grojean, D.E. Groom, M. Grunewald, A. Gurtu, T. Gutsche, H.E. Haber, K. Hagiwara, C. Hanhart, S. Hashimoto, Y. Hayato, K.G. Hayes, M. Heffner, B. Heltsley, J.J. Hernandez-Rey, K. Hikasa, A. Hocker, J. Holder, A. Holtkamp, J. Huston, J.D. Jackson, K.F. Johnson, T. Junk, M. Kado, D. Karlen, U.F. Katz, S.R. Klein, E. Klempt, R.V. Kowalewski, F. Krauss, M. Kreps, B. Krusche, Y.V. Kuyanov, Y. Kwon, O. Lahav, J. Laiho, P. Langacker, A. Liddle, Z. Ligeti, C.J. Lin, T. M. Liss, L. Littenberg, K.S. Lugovsky, S.B. Lugovsky, F. Maltoni, T. Mannel, A.V. Manohar, W.J. Marciano, A.D. Martin, A. Masoni, J. Matthews, D. Milstead, P. Molaro, K. Monig, F. Moortgat, M.J. Mortonson, H. Murayama, K. Nakamura, M. Narain, P. Nason, S. Navas, M. Neubert, P. Nevski, Y. Nir, L. Pape, J. Parsons, C. Patrignani, J.A. Peacock, M. Pennington, S.T. Petcov, A. Piepke, A. Pomarol, A. Quadt, S. Raby, J. Rademacker, G. Raffelt, B.N. Ratcliff, P. Richardson, A. Ringwald, S. Roesler, S. Rolli, A. Romaniouk, L.J. Rosenberg, J.L. Rosner, G. Rybka, C.T. Achrajda, Y. Sakai, G.P. Salam, S. Sarkar, F. Sauli, O. Schneider, K. Scholberg, D. Scott, V. Sharma, S.R. Sharpe, M. Silari, T. Sjostrand, P. Skands, J.G. Smith, G.F. Smoot, S. Spanier, H. Spieler, C. Spiering, A. Stah, T. Stanev, S.L. Stone, T. Sumiyoshi, M.J. Sphers, F. Takahashi, M. Tanabashi, J. Terning, L. Tiator, M. Titov, N.P. Tkachenko, N.A. Tornqvist, D. Tovey, G. Valencia, G. Venanzoni, M.G. Vincter, P. Vogel, A. Vogt, S.P. Wakely, W. Walkowiak, C.W. Walter, D.R. Ward, G. Weiglein, D.H. Weinberg, E.J. Weinberg, M. White, L.R. Wiencke, C.C. Woh, L. Wofenstein, J. Womersley, C.L. Woody, R.L. Workman, A. Yamamoto, W.M. Yao, G.P. Zeller, O.V. Zenin, J. Zhang, R.Y. Zhu, F. Zimmermann, P.A. Zyla, G. Harper, V.S. Lugovsky, P. Schaffner, P.D. Grp, Review of particle physics particle data group, Chin. Phys. C 38 (2014).
[24] G.R. Lynch, O.I. Dahl, Approximations to multiple Coulomb scattering, Nucl. Instr. Meth. B 58 (1991) 6–10.
[25] <https://www.wolframalpha.com>, <http://physics.nist.gov/PhysRefData>.
[26] B. Rossi, High Energy Particles, Prentice-Hall Inc, Englewood Cliffs, NJ, 1952.
[27] H. Bichsel, A method to improve tracking and particle identification in TPCs and silicon detectors, Nucl. Instr. Meth. A 562 (2006) 154–197.
[28] H. Bethe, Zur Theorie des Durchgangs schneller Korpuskularstrahlen durch Materie, Ann. Phys. 5 (1930) 325.
[29] D.E. Groom, N.V. Mokhov, S.I. Striganov, Muon stopping power and range tables 10 MeV-100 TeV, At. Data Nucl. Data Tables 78 (2001) 183–356.

[30] D.Y. Ivanov, E.A. Kuraev, A. Schiller, V.G. Serbo, Production of e(+)e(−) pairs to all orders in Z alpha for collisions of high-energy muons with heavy nuclei, Phys. Lett. B 442 (1998) 453–458.
[31] D.E. Groom, N.V. Mokhov, S.I. Striganov, Muon stopping powers and range tables: 10 MeV–100 TeV, At. Data Nucl. Data Tables 78 (2001) 183–356.
[32] J.L. Wiza, Microchannel plate detectors, Nucl Instr. Meth. 162 (1979) 587–601.
[33] R.P. Tornow, A new method to measure and increase the detection efficiency of a microchannel plate for 100-Kev electrons, Meas. Sci. Technol. 1 (1990) 576–580.
[34] Y.T. Tanaka, I. Yoshikawa, K. Yoshioka, T. Terasawa, Y. Saito, T. Mukai, Gamma-ray detection efficiency of the microchannel plate installed as an ion detector in the low energy particle instrument onboard the GEOTAIL satellite, Rev. Sci. Instr. 78 (2007).
[35] J. Allison, K. Amako, J. Apostolakis, H. Araujo, et al., Geant4 developments and applications, IEEE Trans. Nucl. Sci. 53 (2006) 270–278.
[36] G. Santin, V. Ivanchenko, H. Evans, P. Nieminen, E. Daly, GRAS: a general-purpose 3-D modular simulation tool for space environment effects analysis, IEEE Trans. Nucl. Sci. 52 (2005) 2294–2299.
[37] H.O. Funsten, R.W. Harper, E.E. Dors, P.A. Janzen, B.A. Larsen, E.A. MacDonald, D.I. Poston, S.M. Ritzau, R.M. Skoug, T.H. Zurbuchen, Comparative response of microchannel plate and channel electron multiplier detectors to penetrating radiation in space, IEEE Trans. Nucl. Sci. 62 (2015) 2283–2293.
[38] G.W. Fraser, X-ray and gamma-ray imaging using microchannel plates, Nucl. Instr. Meth. A 221 (1984) 115–130.
[39] G.W. Fraser, The electron detection efficiency of microchannel plates, Nucl. Instr. Meth. Phys. Res. 206 (1983) 445–449.
[40] L. Desorgher, Radiation Simulation Study for the PEP-NU Unit on the LAPLACE Mission, University of Bern, Bern, 2010, pp. 1–33. JGO-PEP-TN-0901.
[41] Juice Team, JUICE environmental specification, Issue 5, JS-14-09 (2015) pp. 49.
[42] K. Singh, H. Singh, V. Sharma, R. Nathuram, A. Khanna, R. Kumar, S.S. Bhatti, H. S. Sahota, Gamma-ray attenuation coefficients in bismuth borate glasses, Nucl. Instr. Meth. B 194 (2002) 1–6.